An Accurate Fourier-Based Method for Three-Dimensional Reconstruction of Transparent Surfaces in the Shape-From-Polarization Method

ZHUANG SUN[ID], YANG QIAO, ZHAOGUO JIANG[ID], XIPING XU[ID], JING ZHOU[ID], AND XUANRUI GONG[ID]
College of Optoelectronic Engineering, Changchun University of Science and Technology, Changchun 130022, China

Corresponding author: Yang Qiao (qiaoyangmilier@hotmail.com)

ABSTRACT The Fourier-based gradient field integration method can efficiently reconstruct transparent surfaces from the measured gradient data in the Shape-from-polarization method. However, for the differentiation operator having large truncation errors and lacking constraints on adjacent heights, it will increase the reconstructing error of the Fourier-based integration method. This paper presents an accurate Fourier-based integration approach to improve the reconstruction accuracy, in which a new differentiation operator is derived by limiting the truncation error and increasing heights and slopes in the operator. In order to modify the data obtained by the new operator to meet the requirements of both periodicity and size for the use of the discrete Fourier transform, we propose a method to extend the raw gradient data by first performing antisymmetric extension and then performing periodic extension. A series of simulations and experiments have been developed to verify the performance of the proposed method. By comparing the approach of this paper with other Fourier-based approaches, including Frankot-Chellappa, Southwell-FT and Simpson-FT, both of the simulation and experiment results show that the proposed Fourier-based integration method performs a higher accuracy than other approaches. In the reconstruction experiment, the reconstruction error can be reduced from $0.065 \sim 0.081$ mm to 0.020 mm for the spherical surface, and from $0.060 \sim 0.12$ mm to 0.016 mm for the free-form surface.

INDEX TERMS Differentiation operator, discrete Fourier transforms, gradient methods, shape-from-polarization, reconstruction algorithms.

I. INTRODUCTION

The acquisition of three-dimensional transparent surfaces is a very challenging topic in three-dimensional inspection and reconstruction [1], [2]. Affected by global light transport and low surface albedo, transparent surfaces still pose difficulties for classical active structured light scanning. It is also hard for stereo vision due to few texture features [3]. Current rendering methods for reconstructing such surfaces mainly include reflection-based methods (such as the Shape-from-polarization method [4], [5] and the Shape-from-distortion

method [6]–[8]) and transmission-based methods (such as direct ray measurement [9], Shape from time of flight [10], and tomography [11]). The Shape-from-polarization method is a widely studied method that establishes the relationship between the surface normal and the polarization state of reflected light [12], [13]. It consists of two steps: polarization analysis and gradient field integration. The main problem currently being studied for this method is how to eliminate zenith angle ambiguity and azimuth ambiguity in polarization analysis. Morel *et al.* [14] proposed to use active illumination to select the correct azimuth angle. Stolz *et al.* [15] introduced a multispectral approach for estimating the appropriate value of zenith angle. Garcia *et al.* [16] utilized circularly

---

The associate editor coordinating the review of this manuscript and approving it for publication was Jenny Mahoney.

polarized light to solve for the zenith ambiguity. Gradient field integration is another essential process that reconstructs the surface from the measured gradient data, which directly affects the accuracy of the reconstructing results. The Frankot-Chellappa method [17] is commonly used in the Shape-from-polarization method. Due to the use of the fast Fourier transform, it has the advantages of fast calculation speed and high reconstruction efficiency. It uses the finite center difference as the differentiation operator to establish the difference-slope relationship. However, the operator has a large truncation error and lacks constraints on adjacent heights, which results in an increase in reconstruction errors.

At present, a variety of gradient field integration methods mainly for two-dimensional gradient data have been proposed and discussed in wavefront and surface reconstruction, which can be roughly separated into two groups, zonal and modal approaches [18], [19]. The zonal approach reconstructs the surface based on the relationship between heights and slopes within the local area. Its basic models include Fried [20], Hudgin [21], and Southwell [22]. The Southwell model estimates the shape at the same rectangular grid where the slopes are obtained [23]. So it can be applied to surface reconstruction easily. Huang and Asundi [24] pointed out a biquadratic surface constraint in the Southwell model, and raised an integration method with iterative compensations to improve the reconstructing accuracy. Li *et al.* [25] proposed a method with the higher-order truncation error to reduce the impact of the constraint on accuracy. The modal approach represents a surface or wavefront as a linear combination of orthogonal basis such as complex exponential function [26]–[28], radial basis function [29], Zernike polynomial [30], [31] and Chebyshev polynomial [31]. The Fourier-based algorithm is a simple and fast method, which takes a complex exponential function as a basis and expands the surface into the spatial-frequency domain. The Frankot-Chellappa method mentioned above is one of such methods. In [32], Freischlad and Koliopoulos introduced the Southwell differentiation operator into the Fourier-based approach (denoted as Southwell-FT). Bahk [33] applied the Simpson operator to the Fourier-based method for reconstructing the wavefront (denoted as Simpson-FT). The operator has a small truncation error but also lacks constraints on adjacent heights. In addition, the application of DFT requires input data to meet the periodicity and rectangular array conditions. Bon *et al.* [34] antisymmetrized the derivative data to satisfy the periodicity and reduce the boundary artifact. For the reconstruction in the general shape area, Roddier and Roddier [35] introduced a Gerchberg-like method to iteratively calculate heights in the non-rectangular region, and Bond *et al.* [36] added constraints to modify this method.

As far as the differentiation operator is concerned, the large truncation error and the lack of relationship between adjacent heights have a bad influence on the reconstructing results. In the paper, based on the finite center difference operator, we derive a new differentiation operator by increasing heights and slopes in the operator and limiting the truncation error,

to improve the accuracy of the Fourier-based method for integrating the heights from the discrete gradients (denoted as ADO-FT). It contains the constraint on the height relationship between adjacent sampling points. At the same time, in order to make the data calculated by the new operator to satisfy the requirements of the discrete Fourier transform, a method of extending the gradient data is proposed in combination with the antisymmetric extension and the periodic condition. For reconstructing the surface in a non-rectangular area, we introduce the Gerchberg route into the proposed method to iteratively calculate heights.

The paper is organized as follows. The second part briefly introduces the principle of polarization analysis for measuring the normal vector, and elaborates on the derivation of the accurate differentiation operator, the extension method and the non-rectangular data reconstruction method. The third and fourth parts analyze the performance of our method through simulations and experiments respectively. The whole work is summarized at the fifth part.

II. ACCURATE FOURIER-BASED METHOD APPLIED IN THE SHAPE-FROM-POLARIZATION METHOD

The Shape-from-polarization method consists of two main steps. Firstly, the normal vector of the transparent surface at each sampling point is measured by polarization analysis. Secondly, the gradient field integration method is used to calculate the depth cues of the reconstructed surface from the measured normal vector. We will introduce the polarization analysis method in Section II.A, and describe the proposed Fourier-based gradient field integration method in Section II.B. In Section II.C, we will explain how to apply the accurate Fourier-based method to the Shape-from-polarization method.

A. POLARIZATION ANALYSIS METHOD FOR MEASURING THE NORMAL VECTOR

When unpolarized light is incident on the surface of an object, the reflected light will change into partially polarized light, and its polarization state is decided by the incident angle and the refractive index of the object. Based on this characteristic, the Shape-from-polarization method measures the normal vector and reconstructs the transparent surface. The principle of Shape-from-polarization method is shown in Fig. 1. The zenith angle θ (incident angle) and the azimuth angle ϕ at the sampling point are the key parameters for determining the normal vector $\vec{N}$.

Generally, the camera is selected as a receiving device. Each pixel corresponds to a sampling point on the measured surface. A rotating polarizer is placed in front of the camera to measure the polarization state of the reflected light. The relationship between the transmitted light intensity I and the rotating angle α of the transmitted axis relative to the y-axis is given by (1).

$$I(\alpha) = \frac{I_{\max} + I_{\min}}{2} + \frac{I_{\max} - I_{\min}}{2} \cos(2\alpha - 2\varphi) \quad (1)$$
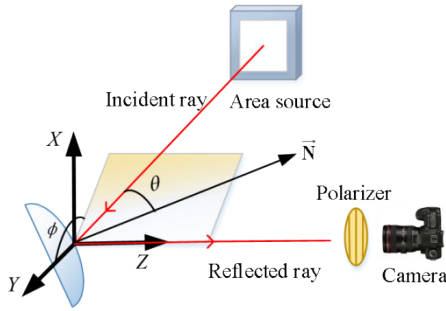
FIGURE 1. Schematic of the Shape-from-polarization method.

where φ is the angle of polarization, I_{max} and I_{min} are the maximum intensity and the minimum intensity, respectively.

According to Snell's law, the incident angle θ can be calculated by the degree of polarization ρ as shown in (2).

$$\rho = \frac{I_{max} - I_{min}}{I_{max} + I_{min}} = \frac{2 \sin \theta \tan \theta \sqrt{n_r^2 - \sin^2 \theta}}{n_r^2 - \sin^2 \theta + \sin^2 \theta \tan^2 \theta} \quad (2)$$

where n_r is the relative refractive index.

The relationship between the azimuth angle ϕ and the angle of polarization φ is as follows

$$\phi = \varphi \pm 90° \quad (3)$$

In Fig. 1, the paper uses a triangulation system [38]. We need to limit the opening angle between the area light source and the camera to be less than the double Brewster angle. The zenith angle is equal to the value less than Brewster angle in two candidate values. Since the entire incident rays are on the same side relative to the camera, the angle corresponding to the other side can be eliminated when calculating the azimuth angle.

The normal vector $\overrightarrow{N}$ or the gradient $(\partial Z(x,y)/\partial x, \partial Z(x,y)/\partial y)$ can be calculated by (4).

$$\overrightarrow{N} = \begin{pmatrix} \tan\theta \cos\phi \\ \tan\theta \sin\phi \\ 1 \end{pmatrix} = \begin{pmatrix} -\partial Z(x,y)/\partial x \\ -\partial Z(x,y)/\partial y \\ 1 \end{pmatrix} \quad (4)$$

where $Z(x, y)$ indicates the height of the surface in the Cartesian coordinate system.

B. THE ACCURATE FOURIER-BASED GRADIENT FIELD INTEGRATION METHOD

1) HIGH-PRECISION DIFFERENTIATION OPERATOR

Due to the convenience and efficiency of the fast Fourier transform, the complex exponential function is selected as the orthogonal basis. The expansion in the frequency domain is equivalent to an inverse discrete Fourier transform [32]. The height and expansion coefficient form a Fourier transform

pair and their relationship is given by

$$Z(m, n) = \frac{1}{MN} \sum_{p=0}^{M-1} \sum_{q=0}^{N-1} \overline{Z}(p, q) \exp[2\pi i(\frac{pm}{M} + \frac{qn}{N})] \quad (5)$$

$$\overline{Z}(p, q) = \sum_{m=1}^{M} \sum_{n=1}^{N} Z(m, n)$$
$$\times \exp\{-2\pi i[\frac{(m-1)p}{M} + \frac{(n-1)q}{N}]\} \quad (6)$$

where $Z(m, n)$ is the height value at the (m, n) point; $\overline{Z}(p, q)$ is the expansion coefficient of $Z(m, n)$ on the Fourier domain; The M and N are the number of sampling points in the y direction and the x direction, respectively.

To integrate the heights from the discrete gradient data, a differentiation operator for building a connection between $D.(m, n)$ and $S.(m, n)$ is used to calculate the expansion coefficient $\overline{Z}(p, q)$, where $D.(m, n)$ is the difference in the $\cdot$ (indicating x or y) direction and $S.(m, n)$ is a formula for estimating the difference with gradients at discrete samples. In the Frankot-Chellappa algorithm, the differentiation operator in the y direction is constructed by finite central differences as (7), and similarly in the x direction.

$$Z(m + 1, n) - Z(m - 1, n) = 2h_y Z_y(m, n) \quad (7)$$

In (7), h_y is the sampling interval in the y direction, the left side of the equal sign is $D_y(m, n)$ and the right side of the equal sign is $S_y(m, n)$.

The $D.(m, n)$ can be expanded as (8). The expansion coefficient $\overline{Z}(p, q)$ is calculated by minimizing the cost function ε in (9).

$$D.(m, n)$$
$$= \frac{1}{MN} \sum_{p=0}^{M-1} \sum_{q=0}^{N-1} a.(p, q) \overline{Z}(p, q) \exp[2\pi i(\frac{pm}{M} + \frac{qn}{N})] \quad (8)$$

$$\varepsilon$$
$$= \sum_{m,n} |D_x(m, n) - S_x(m, n)|^2 + |D_y(m, n) - S_y(m, n)|^2 \quad (9)$$

$a.(p, q)\overline{Z}(p, q)$ is the expansion coefficient of $D.(m, n)$; $a_x(p, q)$ and $a_y(p, q)$ are $\exp(2\pi iq/N) - \exp(-2\pi iq/N)$ and $\exp(2\pi ip/M) - \exp(-2\pi ip/M)$ in the Frankot-Chellappa algorithm, respectively.

Minimizing ε by least squares, $\overline{Z}(p, q)$ is given by

$$\overline{Z}(p, q) = \frac{a_x^*(p, q)DFT[S_x(m, n)] + a_y^*(p, q)DFT[S_y(m, n)]}{|a_x(p, q)|^2 + |a_y(p, q)|^2} \quad (10)$$

Actually, $S.(m, n)$ is not exactly equal to $D.(m, n)$. Considering the one-dimensional form in the y direction, we calculate $D(m) - S(m)$ at the point m by Taylor series expansion,

in which $D_y(m, n)$ and $S_y(m, n)$ are written as $D(m)$ and $S(m)$, respectively.

$$
\begin{aligned}
D(m) &- S(m) \\
&= Z(m+1) - Z(m-1) - 2hZ'(m) \\
&= Z(m) + Z'(m)h + \frac{Z''(m)h^2}{2} + O(h^2) \\
&\quad - [Z(m) + Z'(m)(-h) + \frac{Z''(m)(-h)^2}{2} + O(h^2)] \\
&\quad - 2hZ'(m) \\
&= O(h^2)
\end{aligned}
\tag{11}
$$

There is a truncation error $O(h^2)$ when fitting $D.(m, n)$ with $S.(m, n)$. It can influence the ε in (9). The smaller the truncation error is, the smaller ε is. Therefore, improving the accuracy of the reconstructing result needs to reduce the truncation error.

For the Southwell-FT method [32], the differentiation operator can be expressed as (12). The truncation error is $O(h^2)$.

$$
Z(m+1) - Z(m) = \frac{h}{2}[Z'(m+1) + Z'(m)]
\tag{12}
$$

For the Simpson-FT method [33], the differentiation operator can be expressed as (13). The truncation error is $O(h^3)$.

$$
Z(m+1) - Z(m-1) = \frac{h}{3}[Z'(m+1) + 4Z'(m) + Z'(m-1)]
\tag{13}
$$

In addition, using a differentiation operator that does not constrain adjacent heights has a bad effect on the reconstruction results. In the Simpson-FT and Frankot-Chellappa methods, the differentiation operator establishes the relationship between point (m+1) and point (m−1). It lacks the constraint on point (m+1) and point (m). After reconstruction, the height position of point (m+1) relative to point (m) is not accurate.

Increasing the number of slopes in the differentiation operator can reduce the truncation error [25]. So we follow the route to improve the differentiation operator based on the finite center difference model. As shown in (14), in order to increase the constraint on adjacent heights, we add a center point (m) to $D(m)$. At the same time, we symmetrically add four slopes to $S(m)$, in order to reduce the truncation error to $O(h^4)$.

$$
\begin{aligned}
AZ(m+1) &+ BZ(m) + CZ(m-1) \\
&= h\,[DZ'(m-2) \\
&\quad + EZ'(m-1) + FZ'(m) + GZ'(m+1) \\
&\quad + HZ'(m+2)]
\end{aligned}
\tag{14}
$$

The left and right sides of (14) are expanded at point (m) through the Taylor series expansion.

Left:

$$
\begin{aligned}
A\{Z(m) &+ Z'(m)h + \cdots + Z^{(5)}(m)h^5/120 + O[(h)^5]\} \\
&+ BZ(m) + C\{Z(m) + Z'(m)(-h) \\
&\quad + \cdots + Z^{(5)}(m)(-h)^5/120 + O[(-h)^5]\}
\end{aligned}
\tag{15}
$$

Right:

$$
\begin{aligned}
Dh\{Z'(m) &+ Z''(m)(-2h) \\
&+ \cdots + Z^{(5)}(m)(-2h)^4/24 + O[(-2h)^4]\} \\
&+ Eh\{Z'(m) + Z''(m)(-h) \\
&+ \cdots + Z^{(5)}(m)(-h)^4/24 + O[(-h)^4]\} \\
&+ FhZ'(m) + Gh\{Z'(m) + Z''(m)h \\
&+ \cdots + Z^{(5)}(m)h^4/24 + O[(h)^4]\} \\
&+ Hh\{Z'(m) + Z''(m)(2h) \\
&+ \cdots + Z^{(5)}(m)(2h)^4/24 + O[(2h)^4]\}
\end{aligned}
\tag{16}
$$

To ensure that the coefficients of $Z(m), \cdots, Z^{(5)}(m)$ on the left are equal to those on the right, let $A = C = 1$, $D = -H$, $E = -G$. The relationship between $D(m)$ and $S(m)$ is derived as (17). When the highest-order derivative of $Z(m)$ is less than the fifth order, $D(m)$ and $S(m)$ are exactly equal.

$$
\begin{aligned}
Z(m+1) &- 2Z(m) + Z(m-1) \\
&= \frac{h}{24}[Z'(m-2) - 14Z'(m-1) \\
&\quad + 14Z'(m+1) - Z'(m+2)]
\end{aligned}
\tag{17}
$$

At this time, $D.(m, n)$ can be expanded into the following formula.

$$
\begin{aligned}
D_x&(m, n) \\
&= \frac{1}{MN} \sum_{p=0}^{M-1} \sum_{q=0}^{N-1} a_x(p, q)\overline{Z}(p, q) \exp[2\pi i(\frac{pm}{M} + \frac{qn}{N})] \\
&= \frac{1}{MN} \sum_{p=0}^{M-1} \sum_{q=0}^{N-1} [\exp(\frac{2\pi i q}{N}) + \exp(-\frac{2\pi i q}{N}) - 2] \\
&\quad \times \overline{Z}(p, q) \exp[2\pi i(\frac{pm}{M} + \frac{qn}{N})]
\end{aligned}
\tag{18}
$$

$$
\begin{aligned}
D_y&(m, n) \\
&= \frac{1}{MN} \sum_{p=0}^{M-1} \sum_{q=0}^{N-1} a_y(p, q)\overline{Z}(p, q) \exp[2\pi i(\frac{pm}{M} + \frac{qn}{N})] \\
&= \frac{1}{MN} \sum_{p=0}^{M-1} \sum_{q=0}^{N-1} [\exp(\frac{2\pi i p}{M}) + \exp(-\frac{2\pi i p}{M}) - 2] \\
&\quad \times \overline{Z}(p, q) \exp[2\pi i(\frac{pm}{M} + \frac{qn}{N})]
\end{aligned}
\tag{19}
$$

2) EXTENSION METHOD COMBINING ANTISYMMETRIC EXPANSION WITH PERIODIC CONDITION

For the $M \times N$ slope matrix, the size of the matrix $D.(m, n)$ estimated directly by the differentiation operator is less than $M \times N$, which does not satisfy the size requirement when using the discrete Fourier transform. The matrix $D.(m, n)$ should be extended to a matrix of the same size as the measured slope matrix. There are some methods based on periodicity to solve the problem [26]–[37], [32]. But it cannot be applied to our proposed differentiation operator that has more than one row or one column needs to be extended.

We plan to periodically extend the slope matrix to calculate the extended $D.(m, n)$. However, if the measured surface is
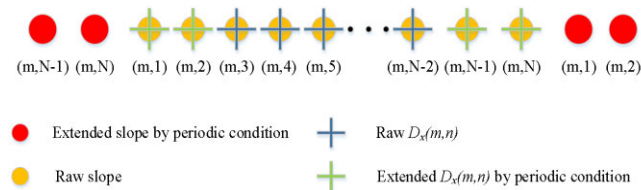
FIGURE 2. Extension of $D_x(m,n)$ in the x direction.

FIGURE 3. Extension from non-rectangular region to rectangular region.

not periodic, directly extending the raw slope matrix cannot obtain a reasonable $D.(m, n)$ at the extended position. So an antisymmetric pre-processing step [34] is required as shown in (20) and (21), which is a process of extending a general surface to a periodic surface.

$$Z_{xe} = \begin{bmatrix} -fliplr\left(flipud\left(Z_x\right)\right) & flipud\left(Z_x\right) \\ -fliplr\left(Z_x\right) & Z_x \end{bmatrix} \quad (20)$$

$$Z_{ye} = \begin{bmatrix} -fliplr\left(flipud\left(Z_y\right)\right) & -flipud\left(Z_y\right) \\ fliplr\left(Z_y\right) & Z_y \end{bmatrix} \quad (21)$$

where $fliplr(-)$ represents columns of matrix $-$ are flipped in the left-right direction, and $flipud(-)$ represents rows of matrix $-$ are flipped in the up-down direction.

After that, we apply the periodic condition to calculate the extended $D.(m, n)$. The slopes of the periodic surface satisfy the relationship in (22) and (23). The M and N are the periods in the y direction and the x direction, respectively. Fig. 2 illustrates the extension of the slope matrix and the $D_x(m, n)$ matrix in the x direction, and the y directions are the same.

$$Z_y(M + m, n) = Z_y(m, n) \quad (22)$$

$$Z_x(m, N + n) = Z_x(m, n) \quad (23)$$

Furthermore, the boundary of the reconstructed surface has a larger error than the inside. The reason is that some slopes in the operator are not measured but filled when solving the $D.(m, n)$ at the boundary position, so that the error increases and the height of the boundary position is abrupt. Therefore, the surface edges need to be recalculated. Here, we take the left side of the reconstructed surface as an example to introduce the recalculation steps as (24) and (25). The Simpson operator [33] is used to obtain the height difference between the two sample points.

$$\Delta x_{1,3} = \frac{h_x}{3} \left(Z'_x(m, 1) + 4Z'_x(m, 2) + Z'_x(m, 3) \right) \quad (24)$$

$$Z(m, 1) = Z(m, 3) - \Delta x_{1,3} \quad (25)$$

3) RECONSTRUCTION IN THE NON-RECTANGULAR AREA

The above is the method of reconstructing the surface in the rectangular region. Since the Fourier-based method requires rectangular data as input, the proposed method cannot directly reconstruct the surface in the general area. For the data in the non-rectangular area, the effective way is to use the Gerchberg route [35], [36], which extends the measured area into a rectangular area as shown in Fig. 3. The data in
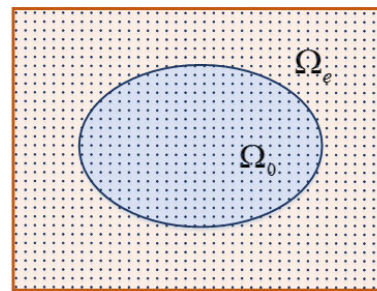
the target area Ω_0 remains unchanged, and other area Ω_e are filled with zero.

After calculating the expansion coefficients of the measured surface, the next step is to get the $D.(m, n)$ in the rectangular area and replace the data in Ω_0 with the original $D.(m, n)$. The heights corresponding to the sampling points within Ω_0 are iteratively calculated until the number of iterations is equal to the limit N_{iter}. The specific calculation steps are as Fig. 4.

C. APPLYING THE ACCURATE FOURIER-BASED METHOD TO THE SHAPE-FROM-POLARIZATION METHOD

In the section, we will describe how to apply the accurate Fourier-based method to the Shape-from-polarization method. This problem is equivalent to how to input the measured gradient data into the Fourier-based gradient integration method to calculate the depth cues. A preparation process is required here to determine the coordinate system in which the measured surface is located. Due to the pinhole model of the camera, the camera coordinate system is not suitable for calculating the height using the Fourier-based gradient integration method. For this problem, we adopt a relaxed perspective model to determine a world coordinate system O-XYZ. Its XOY plane is approximately perpendicular to the reflected ray at each sample point. The conversion relationship between the pixel coordinate system and the world coordinate system is shown in (26) [39]. Through the camera calibration method, the x and y coordinates of the sampling point corresponding to each pixel can be determined in the world coordinate system.

$$\begin{bmatrix} u \\ v \\ 1 \end{bmatrix} = \lambda \begin{bmatrix} \alpha & 0 & u_0 \\ 0 & \beta & v_0 \\ 0 & 0 & 1 \end{bmatrix} \begin{bmatrix} r_1 & r_2 & t \end{bmatrix} \begin{bmatrix} x \\ y \\ 1 \end{bmatrix} \quad (26)$$

where (u, v) is the pixel coordinate in the image plane, λ is a scalar, α, β, u_0, v_0 are intrinsic parameters of the camera, r_1 and r_2 are the 1st and 2nd columns of the rotation matrix, t is the translation matrix, and (x, y) is the sampling point coordinate on the XOY plane of the world coordinate system.

Using the (x, y) coordinates of the sample points and the corresponding gradient $(\partial Z(x,y)/\partial x, \partial Z(x,y)/\partial y)$ as inputs to the ADO-FT method, we can obtain depth cues along the Z axis.
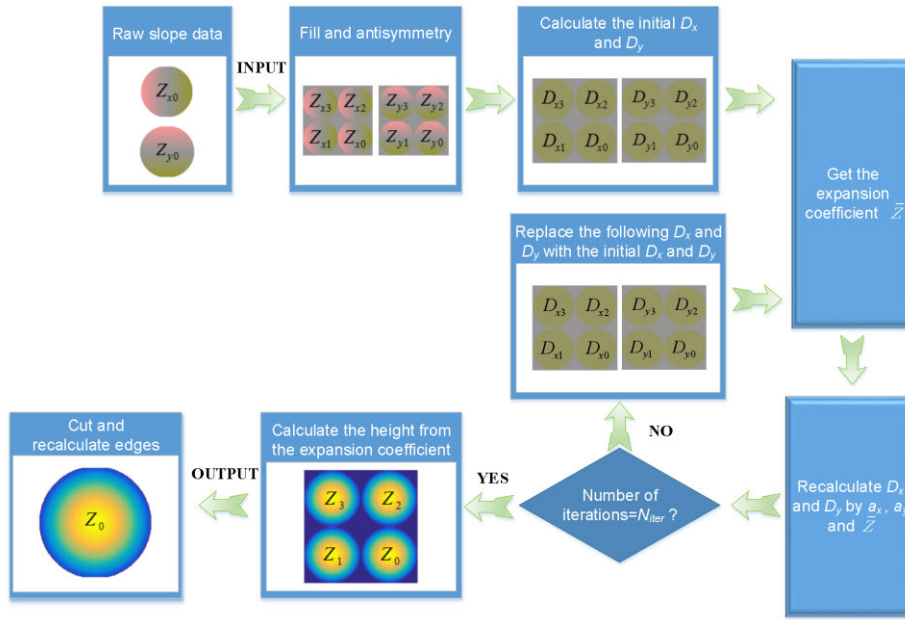
FIGURE 4. The flow chart for reconstructing the surface in a non-rectangular region.

III. SIMULATION

In order to evaluate the performance of the proposed method to reconstruct the surface, a series of simulations are performed to investigate the accuracy, the robustness, and the computing time. We will make the discussion on four aspects as follows.

A. ACCURACY ANALYSIS IN THE RECTANGULAR AREA

The accuracy of the ADO-FT method is discussed and compared with the Frankot-Chellappa, Southwell-FT, and Simpson-FT methods. First, the surfaces represented by (27) and (28) are simulated to investigate the reconstructing results of four algorithms. Equation (27) represents a spherical surface with a radius of 80 mm. Equation (28) is a high-order surface that combines (27) with the fourth, sixth, and eighth order terms. The original surfaces are shown in Fig. 5.

$$Z = \sqrt{80^2 - x^2 - y^2} \tag{27}$$

$$Z = \sqrt{80^2 - x^2 - y^2} + A(x^4 + y^4)$$
$$+ B(x^6 + y^6) + C(x^8 + y^8) + 30 \tag{28}$$

In (27) and (28), (x, y) is the coordinate of the sampling point, Z represents the height of simulated surface, the A, B, and C are -4.71×10^{-5}, -1.56×10^{-8}, and -2.68×10^{-10}, respectively.

The effect of noise is not considered in the section. The surface is reconstructed in the rectangular region from -20 mm to 20 mm both in the x and y directions. There are 200×200 sampling points evenly distributed in the whole area. The spacing (h_x or h_y) between adjacent sampling points is 0.2010 mm. Solving for the partial derivatives of (27) and (28)
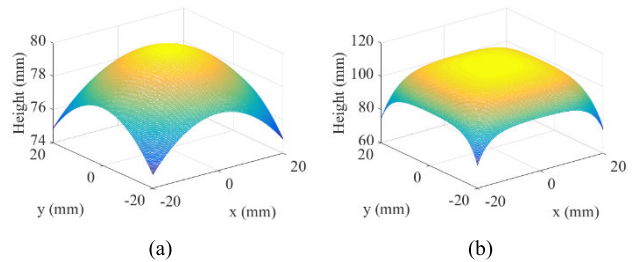

FIGURE 5. The original surfaces: (a) the spherical surface and (b) the higher-order surface.

is to obtain the gradient $(\partial Z(x,y)/\partial x, \partial Z(x,y)/\partial y)$ corresponding to each sampling point, which is used as the input of the four methods. In the ADO-FT method, the measured gradient data are extended by the method of Section II.B.2) for the periodicity required for the discrete Fourier transform. The use of (17) is to calculate the $S_x(m, n)$ and $S_y(m, n)$. According to (8), the expansion coefficient $\overline{Z}(p, q)$ can be obtained, where $a_x(p, q)$ is equal to $\exp(2\pi i q/N) + \exp(-2\pi i q/N) - 2$ and $a_y(p, q)$ is equal to $\exp(2\pi i p/M) + \exp(-2\pi i p/M) - 2$. The piston term $\overline{Z}(0, 0)$ cannot be determined because the denominator of (8) is 0 when both p and q are 0. The piston term has the same effect on the heights of all sample points. So we set it to be 0. The final heights can be acquired by the inverse discrete Fourier transform on the expansion coefficient $\overline{Z}(p, q)$.

The root mean square error (RMSE) is chosen to evaluate the reconstruction error, which is defined as (29).

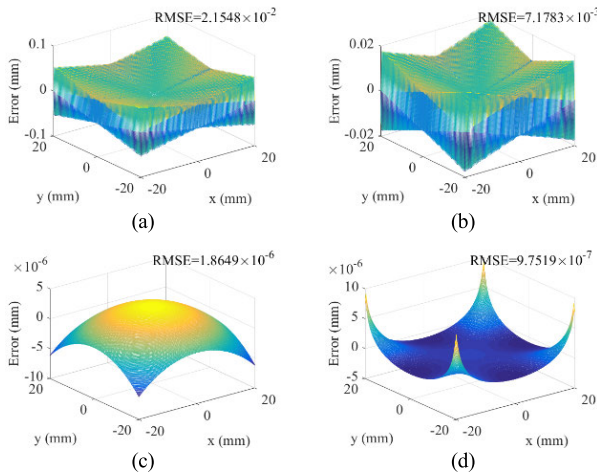$$RMSE = \sqrt{\frac{1}{MN} \sum_{i=1}^{M} \sum_{j=1}^{N} (Z_i - Z_r)^2} \tag{29}$$

FIGURE 6. Reconstruction errors of the spherical surface based on (a) Frankot-Chellapa, (b) Simpson-FT, (c) Southwell-FT, and (d) ADO-FT.

TABLE 1. Reconstructing errors at several sampling points when using the Frankot-Chellappa and Simpson-FT methods to reconstruct the spherical surface.

Frankot-Chellappa		X (mm)			
	-20	-19.7990	-19.5980	-19.3970	-19.1960
Y (mm) 16.9849	-0.0037	0.0492	-0.0032	0.0486	-0.0027
17.1859	-0.0496	0.0038	-0.0486	0.0032	-0.0481
17.3869	-0.0032	0.0498	-0.0027	0.0492	-0.0021
17.5879	-0.0498	0.0033	-0.0492	0.0027	-0.0487

Simpson-FT		X (mm)			
	-20	-19.7990	-19.5980	-19.3970	-19.1960
Y (mm) 16.9849	-0.0011	0.0164	-0.0011	0.0162	-0.0009
17.1859	-0.0162	0.0013	-0.0162	0.0011	-0.0160
17.3869	-0.0009	0.0166	-0.0009	0.0164	-0.0007
17.5879	-0.0164	0.0011	-0.0164	0.0009	-0.0162

TABLE 2. The root mean errors of the Frankot-Chellappa, Southwell-FT, Simpson-FT, and ADO-FT methods when reconstructing the spherical, high-order, and complex surfaces.

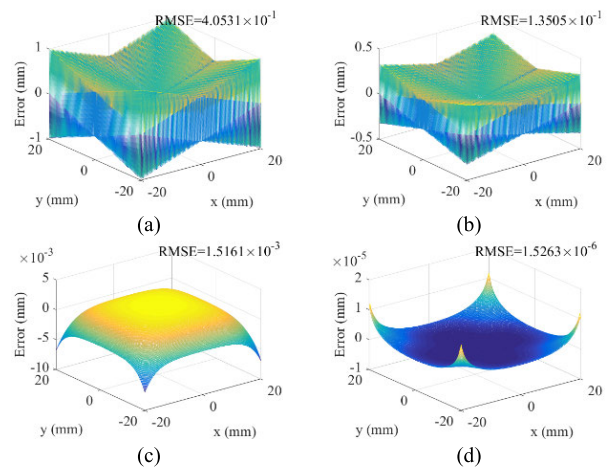| Method	Spherical surface (mm)	High-order surface (mm)	Complex surface (mm)
Frankot-Chellappa	2.1548×10^{-2}	4.0531×10^{-1}	4.3838×10^{-3}
Southwell-FT	1.8649×10^{-6}	1.5161×10^{-3}	1.9333×10^{-4}
Simpson-FT	7.1783×10^{-3}	1.3505×10^{-1}	1.4548×10^{-3}
ADO-FT	9.7519×10^{-7}	1.5263×10^{-6}	2.9200×10^{-5}

FIGURE 7. Reconstruction errors of the high-order surface based on (a) Frankot-Chellapa, (b) Simpson-FT, (c) Southwell-FT, and (d) ADO-FT.

where Z_i is the height of the ideal surface, Z_r is the height of the reconstructed surface.

The reconstructed results of the spherical surface are shown in Fig. 6. The ADO-FT method can reconstruct this surface with high precision ($RMSE = 9.7519 \times 10^{-7}$). The Southwell-FT method can also acquire an accurate reconstructing result. It is because there are no high-order terms in the spherical equation, and the truncation errors ($D.(m, n) - S.(m, n)$) of the differentiation operator are between 7.9708×10^{-10} and 1.0311×10^{-7}. It is small enough. The reconstructing results of the Frankot-Chellappa and Simpson-FT methods are less accurate as shown in Figs. 6(a) and 6(b). Although their truncation errors are small when reconstructing the spherical surface, these lack the constraints on adjacent heights. Table 1 describes the reconstructing errors at several sampling points. We first consider the errors of the Frankot-Chellappa method. According to the differentiation operator, The $(-20, 16.9849)$, $(-19.5980, 16.9849)$, $(-19.1960, 16.9849)$, $(-20, 17.3869)$, $(-19.5980, 17.3869)$, and $(-19.1960, 17.3869)$ belong to a set of related sampling points. The $(-19.7990, 16.9849)$, $(-19.3970, 16.9849)$, $(-19.7990, 17.3869)$, and $(-19.3970, 17.3869)$ belong to another set of related sampling points. The errors of the two sets of sampling points are not at the same level. It can be seen that the relative position between two adjacent reconstructing points is inaccurate. The differentiation operator of the Simpson-FT method is similar to that of the Frankot-Chellappa method, and also lacks the constraints of adjacent points. So its accuracy is also relatively low.

The reconstructing results of the high-order surface are shown in Fig. 7. The surface reconstructed by the ADO-FT method ($RMSE = 1.5263 \times 10^{-6}$) is superior to other methods. Its truncation error is about 7.1554×10^{-10}. As for the Southwell-FT method, its truncation error is about 4.2729×10^{-5}. Due to the influence of the truncation error, the RMSE of the Southwell-FT method is only 1.5161×10^{-3}. Affected by the lack of adjacent height constraints, the accuracy of the Frankot-Chellappa and Simpson-FT methods is lower.

Next, the complex surface in Fig. 8(a) is reconstructed and its height distribution is determined by (30). The ADO-FT method performs better than other methods according to the comparison of Figs 8(b)-8(e). Table 2 summarizes and compares the root mean square errors of the four methods. According to the above simulating results, it can be inferred that the ADO-FT method can effectively improve the reconstruction accuracy by increasing the adjacent point constraints and reducing the truncation error. The Southwell-FT method can still obtain an accurate result when reconstructing the spherical surface. But for the high-order and complex
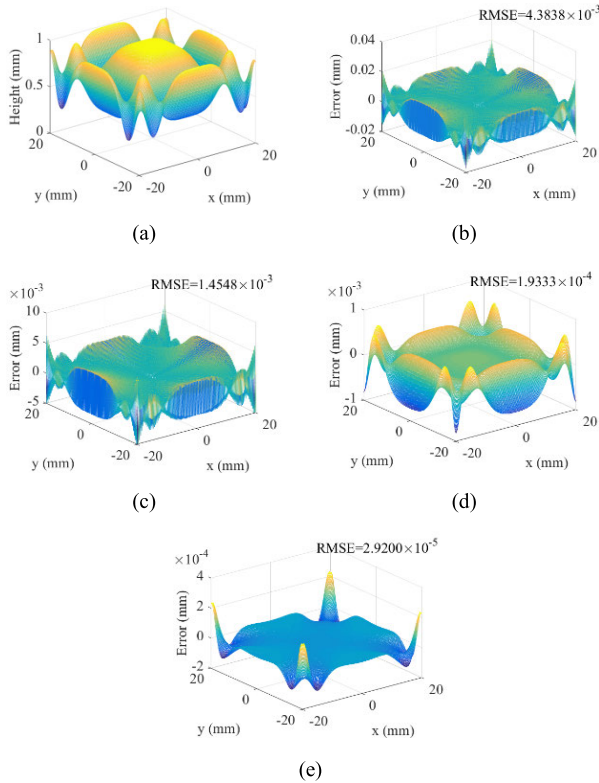
(a)

(b)

(c)

(d)

(e)

FIGURE 8. Reconstruction results of the complex surface: (a) the original surface, (b) the reconstruction error of Frankot-Chellappa, (c) the reconstruction error of Simpson-FT, (d) the reconstruction error of Southwell-FT, and (e) the reconstruction error of ADO-FT.

FIGURE 9. The imaginary part of the height calculated by inverse fast Fourier transform in the ADO-FT method: (a) the spherical surface, (b) the higher-order surface, and (c) the complex surface.

surfaces, the reconstructing accuracy is significantly lower than the ADO-FT method. As for the Frankot-Chellappa and Simpson-FT methods, due to the lack of constraints on adjacent points, the reconstruction results of these are of low accuracy.

$$
\begin{aligned}
Z = {} & \frac{3}{10}\cos(\frac{81x^4}{6.4 \times 10^6} + \frac{9x^2}{8 \times 10^2}) \\
& \times \cos(\frac{81y^4}{6.4 \times 10^6} + \frac{9y^2}{8 \times 10^2}) \\
& + \frac{7}{10}\cos(\frac{81x^4}{1.024\pi \times 10^7} + \frac{9y^2}{6.4\pi \times 10^3})
\end{aligned}
\tag{30}
$$

Furthermore, in the ADO-FT method, due to the complex exponential basis function, the height obtained by inverse fast Fourier transform is usually complex. To solve this problem, the method here is to take the real part of the value and omit the imaginary part. Therefore, the ADO-FT method should satisfy the requirement that the imaginary part of the height calculated by inverse Fourier transform should be as small as possible and close to 0. Fig. 9 shows the imaginary part of the height at each sampling point when reconstructing the above three surfaces using the ADO-FT method. Compared with the corresponding real part, the value is approximately equal to 0.
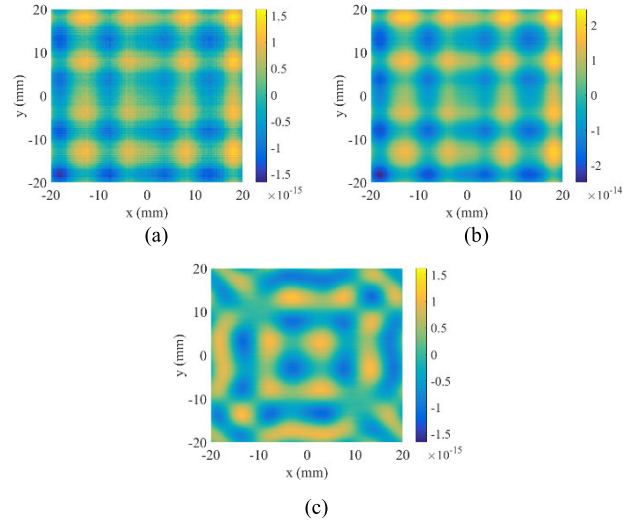
B. EFFECT OF NOISE

Now we describe the effect of noise on accuracy when reconstructing surfaces by using the ADO-FT algorithm. In previous studies, the type of noise added was generally Gaussian noise with zero-mean [30], [31]. Here we also use it. In the section, the complex surface represented by (30) is chosen as the simulated object and different levels of noise are added to the ideal slope data. The noise level is expressed by the signal-to-noise ratio (SNR), which is defined as the ratio of the root mean square (RMS) of ideal slopes to the RMS of noise [25]. We express the SNR in decibels as

$$
SNR = 10\log_{10}(\frac{RMS(Z')}{RMS(N_{noise})})
\tag{31}
$$

where Z' is the ideal x or y gradient, N_{noise} represents the added noise.

In order to quantify the effect of noise on the reconstructing results, the ratio of the RMS of height errors between the reconstructed surface and the ideal surface to the RMS of ideal surface heights is calculated as (32), which is denoted as the normalized reconstruction error E [30].

$$
E = \frac{RMS(Z_r - Z_i)}{RMS(Z_i)}
\tag{32}
$$

where Z_r is the reconstructed surface height, and Z_r is the ideal surface height.

Generally, it is necessary to generate several sets of Gaussian noise at each noise level and add them to the ideal slope data to calculate the corresponding normalized reconstruction error and then average these results, so that a reasonable estimation of E can be obtained [31]. Here we generate 500 sets of noise at each noise level. Fig. 10 shows that when SNR is greater than 7 dB, the normalized reconstruction error E is lower than 0.01.
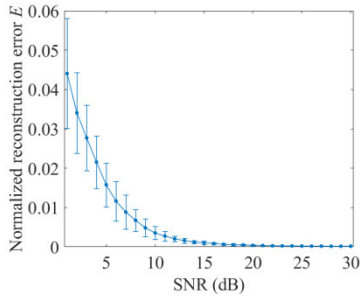
FIGURE 10. The effect of noise on reconstructing accuracy in the ADO-FT method. Plots represent the mean of normalized reconstruction error and error bar in the plot represent the confidence interval.
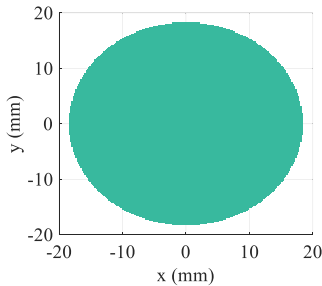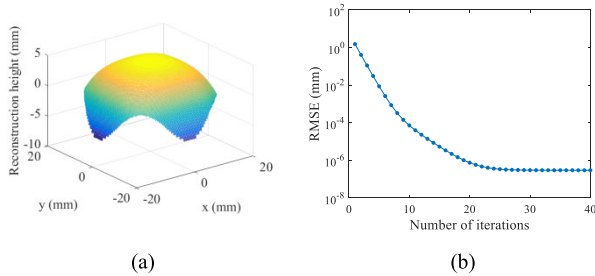

FIGURE 11. Non-rectangular area.

FIGURE 12. Reconstruction results in the non-rectangular region: (a) the reconstructed surface and (b) the relationship between the number of iterations and RMSE.

C. RECONSTRUCTION RESULTS IN THE NON-RECTANGULAR AREA

In the section, we combine the ADO-FT method with the Gerchberg route and verify the reconstructing accuracy of this method in the non-rectangular area. The surface indicated by (28) is simulated and reconstructed in the green area as shown in Fig. 11.

The process of extending a general area into a rectangular area is to extract the x-directional and the y-directional slopes of the green portion and to fill the other portion with 0. We reconstruct the non-rectangular data according to the flow of Fig. 4. After the reconstruction, the height data in the desired area are cut out. Fig. 12(a) shows the reconstructed surface when the number of iterations is 40 and the RMSE at this time is 7.1453×10^{-7} mm. The relationship between the number of iterations and RMSE is shown in Fig. 12(b). When the number of iterations exceeds 30, the reconstructing result tends to be stable.
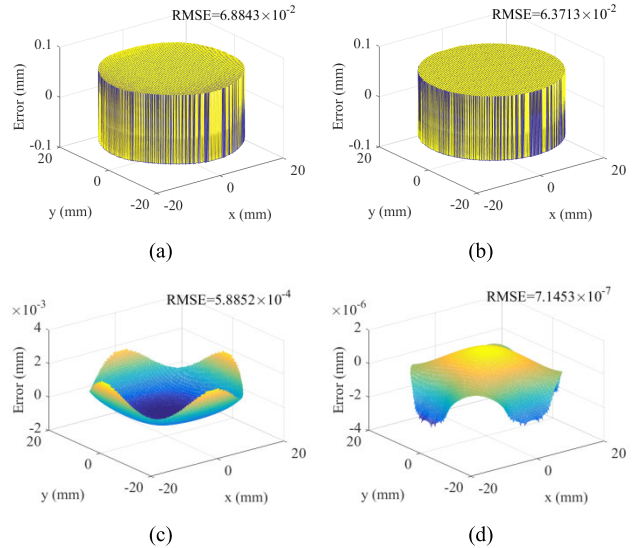

FIGURE 13. Error distribution at all sampling points when using these four methods: (a) Frankot-Chellappa, (b) Simpson-FT, (c) Southwell-FT, and (d) ADO-FT method.

TABLE 3. RMSE and iteration times of four methods in reconstructing non-rectangular data.

Method	RMSE (mm)	Number of iterations
Frankot–Chellappa	6.8843×10^{-2}	40
Southwell-FT	5.8852×10^{-4}	40
Simpson-FT	6.3713×10^{-2}	40
ADO-FT	7.1453×10^{-7}	40

The Frankot-Chellappa, Southwell-FT, and Simpson-FT methods cannot be directly applied to the reconstruction of non-rectangular data. To compare these methods with our method, we introduce the Gerchberg iterative route into these methods for handling the non-rectangular data. The reconstruction processes of these are similar to the process in Section II.B.3). Figure 13 depicts the error distribution at all sampling points when using the four methods. Table 3 describes the root mean square error when the number of iterations is 40. It can be concluded that our method is better than other methods in terms of precision.

D. COMPUTING TIME

In the section, we discuss the computing time of the ADO-FT method. When the measured gradient data is a matrix with M rows and N columns, it has MN elements. In the ADO-FT method, after the antisymmetric extension, the number of elements increases from MN to $4MN$. Let $n = 4MN$. For the ADO-FT method, the computing time of the three parts needs to be analyzed, including the calculations of $D_x(m, n)$ and $D_y(m, n)$, the fast Fourier transform (FFT) on $D_x(m, n)$ and $D_y(m, n)$, and the inverse fast Fourier transform (iFFT) on the expansion coefficient $\overline{Z}(p, q)$. The rest spends less time and can be ignored. Since both $D_x(m, n)$ and $D_y(m, n)$ have n elements, it takes $2n$ operations to calculate $D_x(m, n)$

TABLE 4. Computing time of the four methods.

	Spherical surface	Higher-order surface	Complex surface
Frankot-Chellappa	0.080s	0.076s	0.079s
Southwell-FT	0.081s	0.078s	0.083s
Simpson-FT	0.086s	0.088s	0.085s
ADO-FT	0.094s	0.092s	0.089s

TABLE 5. Calculation time of four methods for non-rectangular data.

Frankot-Chellappa	Southwell-FT	Simpson-FT	ADO-FT
0.947 s	0.886 s	0.923 s	0.899 s

and $D_y(m, n)$. In [36], when using a fast Fourier transform for a matrix with n elements, the number of operations is approximately $n \log n$. So the FFT on $D_x(m, n)$ and $D_y(m, n)$ requires about $2n \log n$ operations, and the iFFT on the expansion coefficient $\overline{Z}(p, q)$ requires about $n \log n$ operations. The number of major operations (N_{op}) during the entire reconstructing process is given by

$$N_{op} = \underbrace{2n}_{\text{Computing } D_x(m,n) \text{ and } D_y(m,n)} + \underbrace{2n \log n}_{\text{FFT for } D_x(m,n) \text{ and } D_y(m,n)}$$
$$+ \underbrace{n \log n}_{\text{iFFT for } \overline{Z}(p,q)} \quad (33)$$

For reconstructing the spherical, higher-order, and complex surfaces of Section III.A, the computing time is shown in Table 4. Each running time result is the average value of 10 repeats in MATLAB (R2016a) with Intel(R) Core(TM) i5-7200U CPU @ 2.50 GHz. The size of the measured gradient data is 200×200. So n is equal to 1.6×10^5. A total of approximately 6.0718×10^6 operations are required to complete the reconstruction for the ADO-FT method. The results show that our method is as fast as the traditional Fourier-based methods.

The number of operations for the non-rectangular reconstruction can be calculated by (34). The Gerchberg route is introduced into the ADO-FT method. It increases the number of operations. In the Gerchberg iteration term, the $4n \log n$ term refers to the number of operations in the forwards and backwards FFTs for $D_x(m, n)$ and $D_y(m, n)$, and the $2n$ term refers to the replacement of the original measurement. The number of sampling points in the target area in Section III.C is 25344. It is extended into the rectangular area, and the number of sampling points is increased to 40000. After the antisymmetric extension, n is equal to 1.6×10^5. When the number of iterations (n_{iter}) is 40, the reconstructing process requires about 3.2180×10^8 operations. It takes about 0.899 seconds. Table 5 depicts the comparison of the four methods with respect to calculation time. The proposed method has almost the same runtime as the traditional
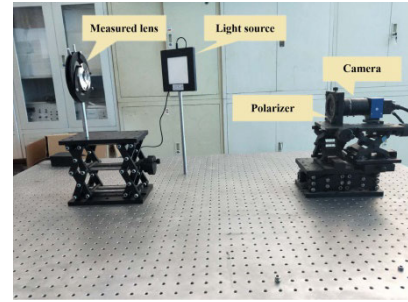

FIGURE 14. Experimental system.

TABLE 6. Specific information about the spherical and free-form lenses.

Spherical lens	
Formula of front surface	$Z = \sqrt{R^2 - x^2 - y^2}$
Coefficient	$R=98.97$
Material	BK7
Refractive index	1.51680
Free-form lens	
Formula of front surface	$Z = -\dfrac{A(x^2 + y^2)}{1+\sqrt{1-(1+k)A^2(x^2+y^2)}}$ $+ B(x^2+y^2)^2 + C(x^2+y^2)^3$ $+ D(x^2+y^2)^4$
Coefficients	$A=1/152.13$, $k=0$, $B=4.5\times10^{-5}$, $C=-8.28\times10^{-8}$, $D=1.06\times10^{-10}$
Material	F5
Refractive index	1.60342

Fourier-based approach.

$$N_{op} = \underbrace{2n}_{\text{Computing } D_x(m,n) \text{ and } D_y(m,n)} + \underbrace{n_{iter}(4n \log n + 2n)}_{\text{Gerchberg iteration}}$$
$$+ \underbrace{n \log n}_{\text{iFFT for } \overline{Z}(p,q)} \quad (34)$$

IV. EXPERIMENT

We carry out a few experiments to evaluate the results of the Frankot-Chellappa, Simpson-FT, Southwell-FT, and ADO-FT methods in the Shape-from-polarization approach. The experimental system consists of a SVS-Vistek SVS285MUCP camera, a rotating linear polarizer and a white area source as shown in Fig. 14. The polarizer is mounted in front of the camera. The camera, the target surface, and the source form a triangulation system for eliminating the azimuth ambiguity. The opening angle between the source and camera is adjusted to about 30°. The purpose is to limit the correct zenith angle to be less than Brewster angle and to exclude the ambiguity value. Moreover, it is easier for the camera to receive the image of the source reflected on the measured surface.

We select the front surface of the free-form lens and the front surface of the spherical lens in Fig. 15 as reconstructing targets. Table 6 describes the specific information of the two lenses. The surfaces within the red rectangle of Fig. 15 are
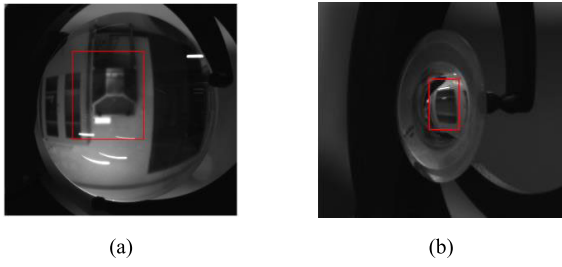
FIGURE 15. Front surfaces of (a) the spherical lens and (b) the free-form lens.
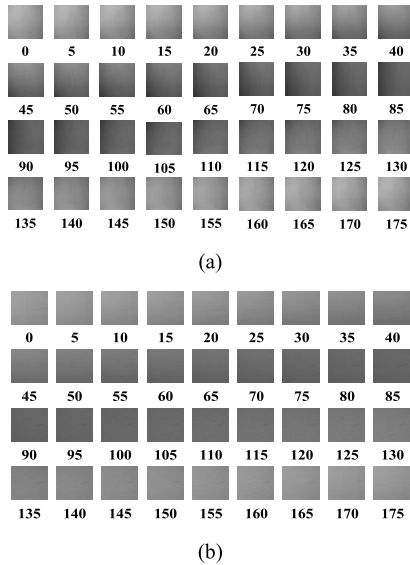

FIGURE 16. Intensity image corresponding to 36 rotation angles in the target area of (a) the spherical surface and (b) the free-form surface.

TABLE 7. Camera extrinsic and intrinsic parameters.

Extrinsic parameters	
Translation vector	T=[-138.209817 -51.935920 1037.106713]

Rotation matrix	R=[0.020573 0.998985 0.040078
	     0.999494 -0.021523 0.023421
	     0.024259 0.039576 -0.998922]

Pixel error	E=[0.16921 0.15695]
Intrinsic parameters	
Focal length	Fc=[3718.60235 3717.69723]$\pm$[32.90398 32.58908]
Principal point	cc=[756.01794 518.06535]$\pm$[19.93498 11.86868]
Distortion	kc=[-0.00659 -4.93301 -0.00203 0.01004 0.00000]
Pixel error	E= [0.17092 0.16754]

reconstructed here to compare the reconstructing accuracy of the four methods.

Firstly, the normal vector corresponding to each pixel is measured by polarization analysis. The polarizer is rotated from 0° to 175° with an interval of 5°, so as to capture 36 images that record the intensity of each pixel in the target area as illustrated in Fig. 16. We fit the variety of the intensity for pixels according to (1) and calculate the degree of polarization ρ and the angle of polarization φ. Then we use the (2)
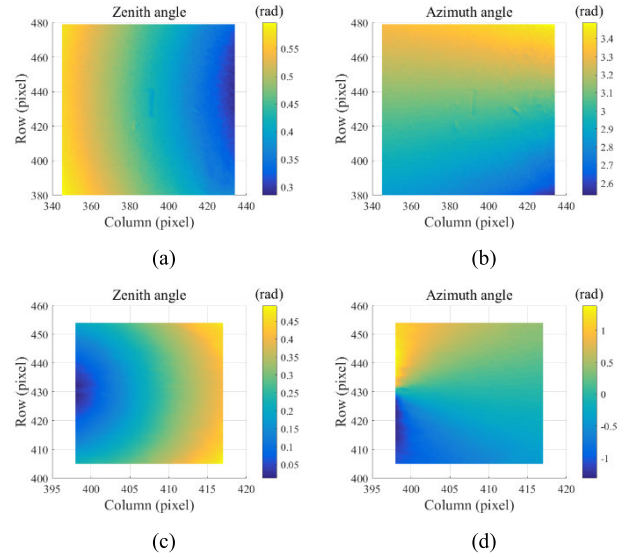

FIGURE 17. False color map about (a) zenith angle and (b) azimuth angle corresponding to the spherical surface, (c) zenith angle and (d) azimuth angle corresponding to the free-form surface.
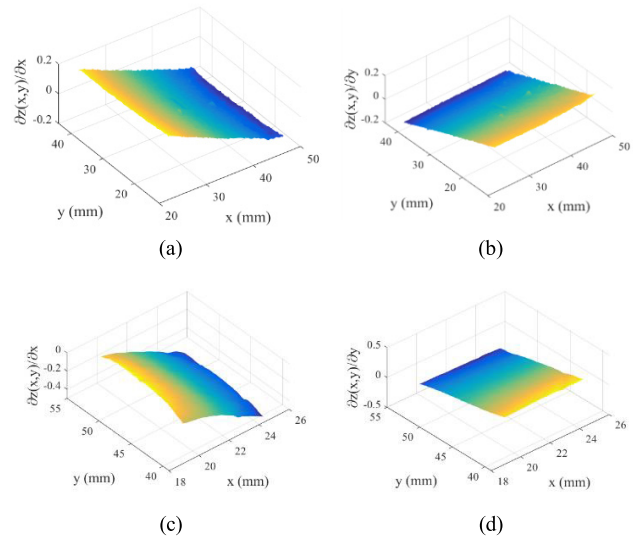

FIGURE 18. The distribution of (a) $\partial Z(x,y)/\partial x$ and (b) $\partial Z(x,y)/\partial y$ for the spherical surface; the distribution of (c) $\partial Z(x,y)/\partial x$ and (d) $\partial Z(x,y)/\partial y$ for the free-form surface.

and (3) to solve the azimuth angle ϕ and the zenith angle θ. The zenith angle and azimuth angle images are depicted using false color scheme in Fig. 17. Subsequently, the normal vector and the gradient ($\partial Z(x,y)/\partial x$, $\partial Z(x,y)/\partial y$) can be obtained by (4).

Secondly, we need to determine the world coordinate system O-XYZ in which the measured surface is located, and calculate the coordinates of the sample points on the XOY plane. Here we use Zhang's camera calibration method [37] to establish the relationship between the pixel coordinate system and the world coordinate system. The calibration results of the camera are shown in Table 7. According to the conversion relationship of the two coordinate systems, the coordinates
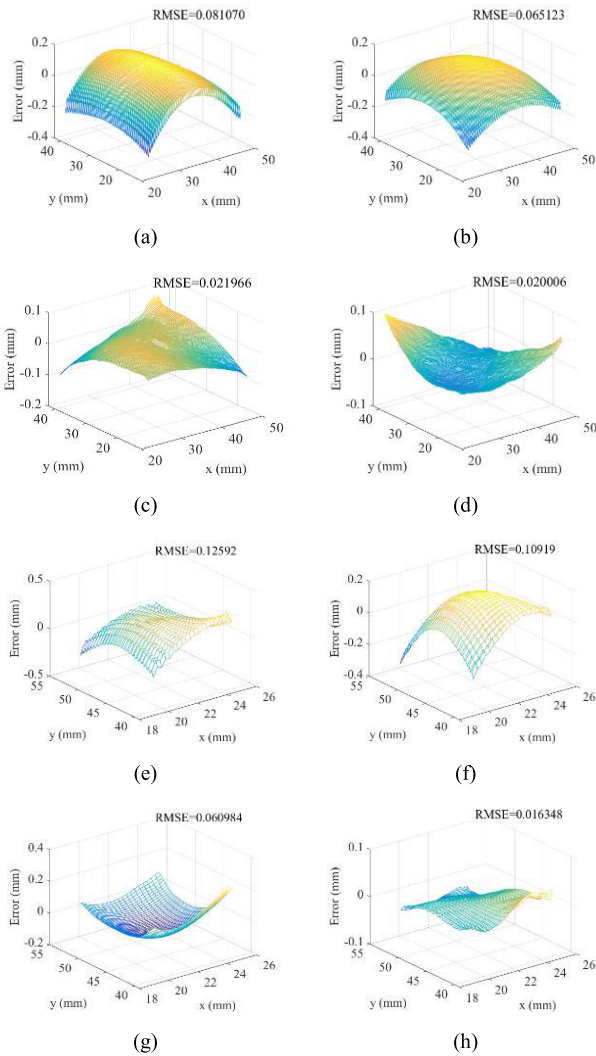
FIGURE 19. Reconstruction errors of the spherical surface based on (a) Frankot-Chellapa, (b) Simpson-FT, (c) Southwell-FT, and (d) ADO-FT, and reconstruction errors of the free-form surface based on (e) Frankot-Chellapa, (f) Simpson-FT, (g) Southwell-FT, and (h) ADO-FT.
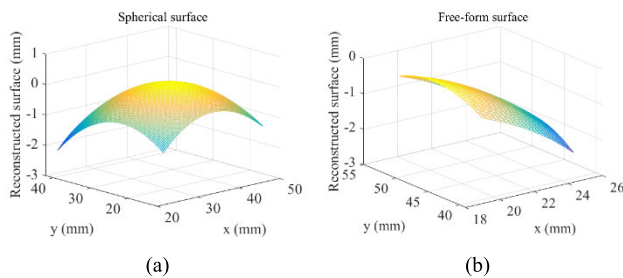

FIGURE 20. Reconstructed surface using ADO-FT method: (a) the spherical surface and (b) the free-form surface.

of the sampling points corresponding to all the pixels can be obtained. The $(\partial Z(x,y)/\partial x, \partial Z(x,y)/\partial y)$ at the sampling point is the $(\partial Z(x,y)/\partial x, \partial Z(x,y)/\partial y)$ measured at the relevant pixel. Fig. 18 depicts the distribution of $\partial Z(x,y)/\partial x$ and $\partial Z(x,y)/\partial y$ at all sampling points.

Thirdly, the coordinate of the sampling point and the corresponding gradient $(\partial Z(x,y)/\partial x, \partial Z(x,y)/\partial y)$ are used as inputs to the four methods to reconstruct the free-form surface and the spherical surface. The reconstructed errors are shown in Fig. 19. For the spherical surface, the ADO-FT method and the Southwell-FT method have smaller errors with RMSEs of 0.020006 mm and 0.021966 mm, respectively. For the free-form surface, the ADO-FT method is significantly better than the other three methods, and its RMSE is 0.016348. The reconstructed surfaces using ADO-FT method are shown in Fig. 20.

V. CONCLUSION

In the paper, we propose an accurate Fourier-based approach to improve the Shape-from-polarization method for reconstructing transparent surfaces. A high-precision differentiation operator is derived by increasing the number of heights and slopes in the operator, which can effectively reduce the truncation error and establish the relationship between adjacent heights. For the periodicity and size requirements corresponding to the new operator, we combine antisymmetric extension with periodic condition to extend the raw measured data. Furthermore, the surface within the non-rectangular region is reconstructed in accordance with the iterative Gerchberg route. A series of simulations have been designed to evaluate the performance of the ADO-FT method in terms of accuracy comparison, effect of noise, reconstruction of non-rectangular data, and computing time. The three common approaches Frankot-Chellappa, Southwell-FT and Simpson-FT were used as comparison to ADO-FT. The reconstruction results show that the proposed method is more accurate than other methods. The processing speed of ADO-FT is as fast as the traditional Fourier-based methods. In the reconstruction experiment, our method can reduce the root mean square error from 0.065 ~ 0.081 mm to 0.020 mm for the spherical surface, and from 0.060 ~ 0.12 mm to 0.016 mm for the free-form surface. It can be concluded that the ADO-FT method is effective and accurate to reconstruct surfaces from gradients. Furthermore, the approach proposed in this paper could also be applied to other methods related to gradient integration, such as the fringe reflection technique and the Shack–Hartmann method.

REFERENCES

[1] F. Drouet, C. Stolz, O. Laligant, and O. Aubreton, ''3D reconstruction of external and internal surfaces of transparent objects from polarization state of highlights,'' *Opt. Lett.*, vol. 39, no. 10, pp. 2955–2958, May 2014.

[2] C. Stolz, A. Zanzouri Kechiche, and O. Aubreton, ''Short review of polarimetric imaging based method for 3D measurements,'' *Proc. SPIE*, vol. 9896, Apr. 2016, Art. no. 98960.

[3] I. Ihrke, K. N. Kutulakos, H. P. A. Lensch, M. Magnor, and W. Heidrich, ''Transparent and specular object reconstruction,'' *Comput. Graph. Forum*, vol. 29, no. 8, pp. 2400–2426, Nov. 2010.

[4] M. Ferraton, C. Stolz, and F. Mériaudeau, ''Optimization of a polarization imaging system for 3D measurements of transparent objects,'' *Opt. Express*, vol. 17, no. 23, Nov. 2009, Art. no. 21077.

[5] D. Miyazaki and K. Ikeuchi, ''Shape estimation of transparent objects by using inverse polarization ray tracing,'' *IEEE Trans. Pattern Anal. Mach. Intell.*, vol. 29, no. 11, pp. 2018–2030, Nov. 2007.

[6] K. N. Kutulakos and E. Steger, "A theory of refractive and specular 3D shape by light-path triangulation," in *Proc. IEEE ICCV*, Beijing, China, Oct. 2005, pp. 1448–1455.

[7] M. Tarini, H. P. A. Lensch, M. Goesele, and H.-P. Seidel, "3D acquisition of mirroring objects using striped patterns," *Graph. Models*, vol. 67, no. 4, pp. 233–259, Jul. 2005.

[8] A. C. Sanderson, L. E. Weiss, and S. K. Nayar, "Structured highlight inspection of specular surfaces," *IEEE Trans. Pattern Anal. Mach. Intell.*, vol. 10, no. 1, pp. 44–55, Jan. 1988.

[9] K. N. Kutulakos and E. Steger, "A theory of refractive and specular 3D shape by light-path triangulation," *Int. J. Comput. Vis.*, vol. 76, no. 1, pp. 13–29, Jan. 2008.

[10] K. Tanaka, Y. Mukaigawa, H. Kubo, Y. Matsushita, and Y. Yagi, "Recovering transparent shape from Time-of-Flight distortion," in *Proc. IEEE Conf. Comput. Vis. Pattern Recognit. (CVPR)*, Las Vegas, NV, USA, Jun. 2016, pp. 27–30.

[11] B. Trifonov, D. Bradley, and W. Heidrich, "Tomographic reconstruction of transparent objects," in *Proc. EGSR*, Nicosia, Cyprus, 2006, pp. 51–60.

[12] D. Miyazaki, M. Kagesawa, and K. Ikeuchi, "Transparent surface modeling from a pair of polarization images," *IEEE Trans. Pattern Anal. Mach. Intell.*, vol. 26, no. 1, pp. 73–82, Jan. 2004.

[13] M. Vedel, N. Lechocinski, and S. Breugnot, "3D shape reconstruction of optical element using polarization," *Proc. SPIE*, vol. 7672, pp. 92–96, Apr. 2010.

[14] O. Morel, C. Stolz, F. Meriaudeau, and P. Gorria, "Active lighting applied to three-dimensional reconstruction of specular metallic surfaces by polarization imaging," *Appl. Opt.*, vol. 45, no. 17, p. 4062, Jun. 2006.

[15] C. Stolz, M. Ferraton, and F. Meriaudeau, "Shape from polarization: A method for solving zenithal angle ambiguity," *Opt. Lett.*, vol. 37, no. 20, p. 4218, Oct. 2012.

[16] N. M. Garcia, I. de Erausquin, C. Edmiston, and V. Gruev, "Surface normal reconstruction using circularly polarized light," *Opt. Express*, vol. 23, no. 11, p. 14391, May 2015.

[17] R. T. Frankot and R. Chellappa, "A method for enforcing integrability in shape from shading algorithms," *IEEE Trans. Pattern Anal. Mach. Intell.*, vol. TPAMI-10, no. 4, pp. 439–451, Jul. 1988.

[18] B. Dong and M. J. Booth, "Wavefront control in adaptive microscopy using Shack-Hartmann sensors with arbitrarily shaped pupils," *Opt. Express*, vol. 26, no. 2, pp. 1655–1669, Jan. 2018.

[19] L. Huang, J. Xue, B. Gao, C. Zuo, and M. Idir, "Zonal wavefront reconstruction in quadrilateral geometry for phase measuring deflectometry," *Appl. Opt.*, vol. 56, no. 18, pp. 5139–5144, Jun. 2017.

[20] D. L. Fried, "Least-square fitting a wave-front distortion estimate to an array of phase-difference measurements," *J. Opt. Soc. Amer.*, vol. 67, no. 3, pp. 370–375, Mar. 1977.

[21] R. H. Hudgin, "Optimal wave-front estimation," *J. Opt. Soc. Amer.*, vol. 67, no. 3, pp. 378–382, Mar. 1977.

[22] W. H. Southwell, "Wave-front estimation from wave-front slope measurements," *J. Opt. Soc. Amer.*, vol. 70, no. 8, pp. 998–1006, Aug. 1980.

[23] L. Huang, M. Idir, C. Zuo, K. Kaznatcheev, L. Zhou, and A. Asundi, "Shape reconstruction from gradient data in an arbitrarily-shaped aperture by iterative discrete cosine transforms in southwell configuration," *Opt. Lasers Eng.*, vol. 67, pp. 176–181, Apr. 2015.

[24] L. Huang and A. Asundi, "Improvement of least-squares integration method with iterative compensations in fringe reflectometry," *Appl. Opt.*, vol. 51, no. 31, pp. 7459–7465, Oct. 2012.

[25] G. Li, Y. Li, K. Liu, X. Ma, and H. Wang, "Improving wavefront reconstruction accuracy by using integration equations with higher-order truncation errors in the southwell geometry," *J. Opt. Soc. Amer. A, Opt. Image Sci.*, vol. 30, no. 7, pp. 1448–1459, Jun. 2013.

[26] P. Liang, J. Ding, Z. Jin, C.-S. Guo, and H.-T. Wang, "Two-dimensional wave-front reconstruction from lateral shearing interferograms," *Opt. Express*, vol. 14, no. 2, pp. 625–634, 2006.

[27] A. Dubra, C. Paterson, and C. Dainty, "Wave-front reconstruction from shear phase maps by use of the discrete Fourier transform," *Appl. Opt.*, vol. 43, no. 5, pp. 1108–1113, Feb. 2004.

[28] L. A. Poyneer, D. T. Gavel, and J. M. Brase, "Fast wave-front reconstruction in large adaptive optics systems with use of the Fourier transform," *J. Opt. Soc. Amer. A, Opt. Image Sci.*, vol. 19, no. 10, pp. 2100–2111, Oct. 2002.

[29] K. Tong, Y. Zheng, Z. Zhang, X. Zhao, B. Zhang, L. Song, L. Wang, C. Wang, and P. Wu, "Model of radial basis functions based on surface slope for optical freeform surfaces," *Opt. Express*, vol. 26, no. 11, pp. 14010–14023, May 2018.

[30] J. Ye, W. Wang, Z. Gao, Z. Liu, S. Wang, P. Benítez, J. C. Miñano, and Q. Yuan, "Modal wavefront estimation from its slopes by numerical orthogonal transformation method over general shaped aperture," *Opt. Express*, vol. 23, no. 20, pp. 26208–26220, Sep. 2015.

[31] I. Mochi and K. A. Goldberg, "Modal wavefront reconstruction from its gradient," *Appl. Opt.*, vol. 54, no. 12, pp. 3780–3785, Apr. 2015.

[32] K. R. Freischlad and C. L. Koliopoulos, "Modal estimation of a wave front from difference measurements using the discrete Fourier transform," *J. Opt. Soc. Amer. A, Opt. Image Sci.*, vol. 3, no. 11, pp. 1852–1861, Nov. 1986.

[33] S.-W. Bahk, "Highly accurate wavefront reconstruction algorithms over broad spatial-frequency bandwidth," *Opt. Express*, vol. 19, no. 20, pp. 18997–19014, Sep. 2011.

[34] P. Bon, S. Monneret, and B. Wattellier, "Noniterative boundary-artifact-free wavefront reconstruction from its derivatives," *Appl. Opt.*, vol. 51, no. 23, pp. 5698–5704, Aug. 2012.

[35] F. Roddier and C. Roddier, "Wavefront reconstruction using iterative Fourier transforms," *Appl. Opt.*, vol. 30, no. 11, pp. 1325–1327, Apr. 1991.

[36] C. Z. Bond, C. M. Correia, J.-F. Sauvage, B. Neichel, and T. Fusco, "Iterative wave-front reconstruction in the Fourier domain," *Opt. Express*, vol. 25, no. 10, pp. 11452–11465, May 2017.

[37] Z. Zhang, "A flexible new technique for camera calibration," *IEEE Trans. Pattern Anal. Mach. Intell.*, vol. 22, no. 11, pp. 1330–1334, Nov. 2000.

[38] X. Xu, Y. Qiao, and B. Qiu, "Reconstructing the surface of transparent objects by polarized light measurements," *Opt. Express*, vol. 25, no. 21, pp. 26296–26309, Oct. 2017.

[39] R. Rantoson, C. Stolz, D. Fofi, and F. Meriaudeau, "3D reconstruction by polarimetric imaging method based on perspective model," *Proc. SPIE*, vol. 7389, Jun. 2009, Art. no. 73890C.

ZHUANG SUN was born in Jilin, China, in 1994. He received the B.S. degree from the Changchun University of Science and Technology, in 2017, where he is currently pursuing the M.S. degree. His research interests include polarization analysis and 3D reconstruction for transparent surfaces.

YANG QIAO is currently an Assistant Professor and a Doctoral Supervisor of instruments science and technology with the Changchun University of Science and Technology. She is interested and working on 3D reconstruction for transparent objects, and VR and AR system design.

ZHAOGUO JIANG received the B.S. degree in mechanical engineering from Tsinghua University, Beijing, China, in 1980, and the Ph.D. degree from the Department of Mechanical Engineering, University of California at Berkeley, Berkeley, USA. His research interests include live color display, optical lighting, and precision machining and manufacturing.

XIPING XU received the B.S. degree in electronic engineering from the Changchun Optics Precision Mechanical School, China, in 1993, and the M.S. and Ph.D. degrees from the Changchun University of Science and Technology, China, in 1999 and 2004, respectively. He is currently a Professor and a Doctoral Supervisor with the College of Optoelectronic Engineering, Changchun University of Science and Technology. His research interests include image processing, signal processing, photoelectric detection technology, and modern photoelectric sensing technology.

JING ZHOU received the B.S. degree from the College of Optical and Electronic Information, Changchun University of Science and Technology, in 2017. He is currently pursuing the M.S. degree with the Changchun University of Science and Technology. His research interest is optical design.

XUANRUI GONG received the B.S. degree in photoelectric information science and engineering from Henan Normal University, China, in 2017. She is currently pursuing the Ph.D. degree with the Changchun University of Science and Technology. Her research interests include the target recognition and target tracking with the catadioptric camera.

● ● ●